

Structure and motifs of iron oxides from 1 to 3 TPa

Feng Zheng,¹ Yang Sun^{1,2,*} Renhai Wang^{1,3} Yimei Fang,¹ Feng Zhang,⁴ Bo Da,⁵ Shunqing Wu,^{1,†} Cai-Zhuang Wang,⁴ Renata M. Wentzcovitch,^{2,6,7,‡} and Kai-Ming Ho⁴

¹Department of Physics, OSED, Key Laboratory of Low Dimensional Condensed Matter Physics (Department of Education of Fujian Province), Jiujiang Research Institute, Xiamen University, Xiamen 361005, China

²Department of Applied Physics and Applied Mathematics, Columbia University, New York, New York 10027, USA

³School of Physics and Optoelectronic Engineering, Guangdong University of Technology, Guangzhou 510006, China

⁴Department of Physics, Iowa State University, Ames, Iowa 50011, USA

⁵Research and Services Division of Materials Data and Integrated System, National Institute for Materials Science, 1-1 Namiki, Tsukuba, Ibaraki 305-0044, Japan

⁶Department of Earth and Environmental Sciences, Columbia University, New York, New York 10027, USA

⁷Lamont–Doherty Earth Observatory, Columbia University, Palisades, New York 10964, USA



(Received 27 October 2021; accepted 7 April 2022; published 25 April 2022)

Iron oxides are fundamental components of planet-forming materials. Understanding the Fe-O system's behavior and properties under high pressure can help us identify many new phases and states possible in exoplanetary interiors, especially terrestrial ones. Using the adaptive genetic algorithm, we investigate the structure of iron oxides for a wide range of stoichiometries ($0.25 \leq x_O \leq 0.8$) at 1, 2, and 3 TPa. Five ground-state structures with Fe_2O , FeO , Fe_3O_5 , FeO_2 , and FeO_4 compositions are identified. Phonon calculations confirm their dynamical stability. The *ab initio* molecular dynamics simulations confirm the thermal stability of Fe-rich phases at high temperatures. The calculated density of states suggests that, except for FeO_4 , all phases are metallic, but their carrier densities decrease with increasing pressure and oxygen content. The cluster alignment analysis of stable and metastable phases shows that several motifs may coexist in a structure of iron oxides with low O content. In contrast, most iron oxides with high O content adopt a simple bcc motif at TPa pressures. Our results provide a crystal structure database of iron oxides for modeling and understanding the interiors of exoplanets.

DOI: 10.1103/PhysRevMaterials.6.043602

I. INTRODUCTION

Iron and oxygen are the two most significant elements of Earth-like exoplanets [1]. Studies on iron oxides' structures and fundamental properties provide a valuable understanding of exoplanet-forming phases, particularly terrestrial ones. Their high-pressure behavior has received considerable attention to advance the understanding of Earth's interior. So far, at ambient or low pressures, three basic iron oxides have been known, i.e., wüstite FeO [2], magnetite Fe_3O_4 [3,4], and hematite Fe_2O_3 [5,6]. Previous studies revealed that these three iron oxides undergo complex electronic [7], magnetic [7,8], and structural transformations [8–10] at high pressure, which can not only lead to seismic anomalies but also affect geochemical processes in Earth's interior [9,10]. Besides the three basic iron oxides, several new stoichiometries of compounds were also synthesized at high pressure, such as Fe_4O_5 [11], Fe_5O_6 [12], Fe_5O_7 [10], and Fe_7O_9 [13], suggesting a complex phase diagram of iron oxides. Recently, using *ab initio* random structure searching (AIRSS), Weerasinghe *et al.*

identified a series of stable and metastable Fe-O compounds at 100, 350, and 500 GPa [14], which further broadens the database of the Fe-O system at high pressure. It is worth noting that the predicted pyrite-type FeO_2 was later confirmed by experimental synthesis [15]. This successful discovery is impactful and demonstrates that computational predictions can play a significant role in discovering high-pressure phases.

However, up to now, most attention has been focused on elucidating the nature of structures and phase transitions of iron oxides below 500 GPa. A legitimate question is this: What are the subsequent high-pressure phases of iron oxides? The answer can provide insights into the types of coordination preferred by iron in planet-forming silicates and oxides and possible, stable phases in solid parts of terrestrial planetary cores where pressures can reach ~ 4 TPa [16]. These exoplanets frequently referred to as “super-Earths” [17], have an interior structure and composition similar to Earth, which is dominated by the elements Fe and O [1,17]. Modeling and understanding these planetary interiors can help us investigate their potential habitability, but it requires a basic knowledge of planet-forming phases and their properties under extreme conditions.

In this paper, using an adaptive genetic algorithm (AGA) [18], we study the Fe-O compounds at 1, 2, and 3 TPa across a wide range of stoichiometries ($0.25 \leq x_O \leq 0.8$). The phase

*yangsun@iastate.edu

†wsq@xmu.edu.cn

‡rmw2150@columbia.edu

stability and electronic properties of five ground-state Fe-O structures are investigated. The local packing motifs in these stable and metastable Fe-O compounds are also analyzed as a function of O contents.

II. COMPUTATIONAL METHODS

In this work, Fe-O's crystal structures were determined using the AGA method [18], which combines fast structure exploration by auxiliary classical potentials and the accurate *ab initio* calculations adaptively and iteratively. The Fe and O atoms' initial atomic positions were randomly generated in the GA loop without assuming the Bravais lattice type, symmetry, atom basis, or unit cell dimensions. The total structure pool in our GA search was set to be 128. Structure searches with auxiliary interatomic potentials were performed on 500 consecutive GA generations. Then, the 16 lowest-enthalpy structures at the end of each GA search were selected for single point DFT calculations according to the AGA procedure [18], whose energies, force, and stress are used to adjust the interatomic potential parameters for the next iteration of GA search. A total of 40 adaptive iterations was performed to obtain the final structures.

Here, the embedded-atom method (EAM) [19] was used as the classical auxiliary potential. In EAM, the total energy of an N -atom system was evaluated by

$$E_{\text{total}} = \frac{1}{2} \sum_{i,j(i \neq j)}^N \phi(r_{ij}) + \sum_i F_i(n_i), \quad (1)$$

where $\phi(r_{ij})$ denotes the pair repulsion between atoms i and j with a distance of r_{ij} ; $F_i(n_i)$ is the embedded term with electron density term $n_i = \sum_{j \neq i} \rho_j(r_{ij})$ at the site occupied by atom i . The fitting parameters in the EAM formula were chosen as follows: The parameters for Fe-Fe interactions were taken from the literature [20], while the Fe-O and O-O interactions were modeled by Morse function,

$$\phi(r_{ij}) = D[e^{-2\alpha(r_{ij}-r_0)} - 2e^{-\alpha(r_{ij}-r_0)}], \quad (2)$$

where D , α , and r_0 are fitting parameters. The density function for O atoms is modeled by an exponentially decaying function,

$$\rho(r_{ij}) = \alpha \exp[-\beta(r_{ij} - r_0)], \quad (3)$$

where α and β are fitting parameters. The form proposed by Banerjea and Smith in Ref. [21] was used as the embedding function with fitting parameters F_0 , γ as

$$F(n) = F_0[1 - \gamma \ln n]n^\gamma. \quad (4)$$

For Fe, the density function and embedding function parameters were taken from Ref. [20]. The potential fitting was performed by the force-matching method with a stochastic simulated annealing algorithm as implemented in the POTFIT code [22,23].

First-principles calculations were carried out by using the QUANTUM ESPRESSO (QE) code [24,25]. Our calculations suggest that the spin-polarized state is unstable at ultrahigh pressures for the Fe-O system. As shown in Fig. S1 in the Supplemental Material [26] (also see Ref. [27]), Fe_xO_y compounds with finite magnetic moments always shows much

higher enthalpies than the nonmagnetic solution. This can be attributed to the enhancement of the overlap of the atomic wave functions at ultrahigh pressures, which broadens the Fe d bands and destroys the magnetic order. For this reason, the non-spin-polarized generalized-gradient approximation (GGA) parametrized by the Perdew-Burke-Ernzerhof formula (PBE) was used to describe the exchange-correlation energy. The pseudopotentials for Fe and O were generated by Vanderbilt's method [28] with the valence electronic configuration of $3s^23p^63d^{6.5}4s^1$ and $2s^22p^4$, respectively. These potentials were tested and previously used in a few studies [29] at terapascal pressures, and showed consistent results with the all-electron full-potential calculations for Fe-O phases at 1–3 TPa (see Supplemental Material [26]). A kinetic-energy cutoff of 50 Ry for wave functions and 500 Ry for potentials were used. Brillouin-zone integration was performed over a k -point grid of $2\pi \times 0.03 \text{ \AA}^{-1}$ in the structure refinement. The convergence thresholds are 0.01 eV/ \AA for the atomic force, 0.5 kbar for the pressure, and 1×10^{-5} eV for the total energy. The structural optimization was performed under constant pressure using the Broyden-Fletcher Goldfarb-Shanno (BFGS) algorithm [30–34] with variable cell shape. Phonon dispersions were calculated using the finite displacement method as implemented in the PHONOPY software [35,36].

The *ab initio* molecular dynamics (AIMD) simulations were performed in the canonical (*NVT*) ensemble using the Nosé-Hoover thermostat [37] as implemented in the Vienna *ab initio* simulation package [38,39]. A plane-wave energy cutoff of 450 eV and gamma-only k -point grids were used. The MD time step is 1 fs. All the AIMD simulations start with perfect crystals and run for more than 10 ps. We used a $4 \times 4 \times 2$ supercell (192 atoms) for Fe_2O , a $2 \times 2 \times 3$ supercell (192 atoms) for Fe_3O_5 , a $4 \times 4 \times 4$ supercell (128 atoms) for FeO , a $3 \times 3 \times 2$ supercell (216 atoms) for FeO_2 , and a $3 \times 3 \times 3$ supercell (270 atoms) for FeO_4 in the AIMD simulations.

III. RESULTS AND DISCUSSION

A. AGA search for the Fe-O system

In order to obtain low-enthalpy structures of iron oxides, a wide range of stoichiometries of Fe_xO_y ($x : y = 3 : 1, 2:1, 3:2, 1:1, 4:5, 3:4, 2:3, 3:5, 1:2, 3:7, 1:3, 1:4$) with different formula units (i.e., 1, 2, 3, 4, 5, 6, and 8 f.u.) containing up to 40 atoms is searched at 1, 2, and 3 TPa, respectively. The relative stability of these predicted Fe-O compounds was investigated under the corresponding pressure, depending on the calculated formation enthalpies,

$$\Delta H_f = [H(\text{Fe}_x\text{O}_y) - xH(\text{Fe}) - yH(\text{O})]/(x + y), \quad (5)$$

where H is the calculated enthalpy for a given structure; x and y are the numbers of atoms of Fe and O, respectively. Before we discuss the stable structures of iron oxides, the crystal structures of pure Fe and O should be clarified. For elemental Fe, our calculated results suggest that the Fe-hcp with $P6_3/mmc$ symmetry is the ground-state phase from 1 to 3 TPa, while for oxygen, the $I4_1/acd$ structure [40] is predicted to be stable at 1 and 2 TPa. At 3 TPa, oxygen adopts a structure with $Cmcm$ symmetry [40]. The stable structures of Fe and oxygen are shown in Fig. S2 in the Supplemental

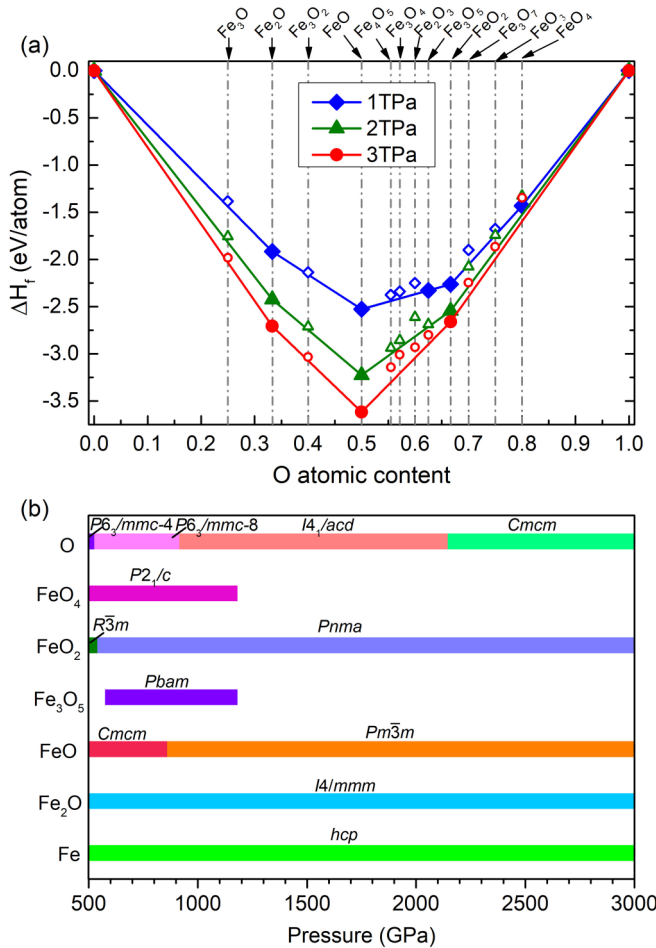


FIG. 1. (a) Convex hull diagrams of the Fe-O system at 1, 2, and 3 TPa. (b) Pressure stability fields of stable phases in the Fe-O system.

Material [26]. Figure 1(a) presents convex hulls of the Fe-O system at 1, 2, and 3 TPa. Five Fe_xO_y stoichiometries are found in these hulls, i.e., Fe_2O , FeO , Fe_3O_5 , FeO_2 , and FeO_4 . As shown in Fig. 1(b), the stability fields of these phases were investigated from 500 GPa to the upper limit for the pressure considered in Ref. [14], to 3 TPa. For Fe_2O , Weerasinghe *et al.* predicted that an $I4/mmm$ phase could be stable from 288 to 500 GPa [14]. Here, we show that it can withstand high pressures up to 3 TPa. Previous DFT calculations show that FeO undergoes a complex structural transformation in the pressure range of the Earth's interior [14,41]. At ultrahigh pressures, our results suggest that the phase with $Cmcm$ symmetry is the ground state from 500 to 860 GPa. At 860 GPa, the $Cmcm$ phase is predicted to transform into a phase of $Pm\bar{3}m$ symmetry (CsCl-type structure), which remains stable up to 3 TPa. Above 575 GPa, the Fe_3O_5 phase is stable in an orthorhombic structure with $Pbam$ symmetry, while, at pressures above 1180 GPa, this phase decomposes into FeO and FeO_2 . For FeO_2 , Weerasinghe *et al.* identified the FeO_2 phase with $Pa\bar{3}$ symmetry [14], which is stable from 100 to 456 GPa. This pyrite-type FeO_2 phase has recently been confirmed by experiments [15]. At 456 GPa, the $Pa\bar{3}$ phase is predicted to transform to a phase with $R\bar{3}m$ symmetry [14].

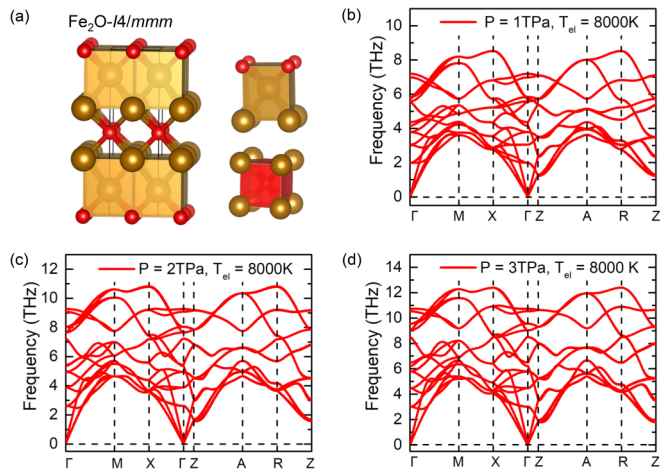


FIG. 2. (a) Crystal structure and Fe and O coordination polyhedra of $I4/mmm$ Fe_2O . Fe and O atoms are denoted by light brown and red spheres, respectively; Phonon dispersions of $I4/mmm$ Fe_2O with $T_{el} = 8000$ K at (b) 1 TPa, (c) 2 TPa, and (d) 3 TPa.

Here, we show that $R\bar{3}m$ FeO_2 should transform to another phase with $Pnma$ symmetry at 540 GPa, and $Pnma$ FeO_2 can be stable to at least 3 TPa. At 500 GPa, FeO_4 adopts a structure with $P2_1/c$ symmetry. At 1180 GPa, $P2_1/c$ FeO_4 decomposes into FeO_2 and O. The structural parameters of these stable iron oxides are listed in Table S1 in the Supplemental Material [26].

B. Crystal structure for stable Fe-O compounds

Fe_2O . Figure 2 shows the crystal structure and phonon dispersion for tetragonal Fe_2O with $I4/mmm$ symmetry. In this structure, each Fe is coordinated to four Fe's and four O's, while each O is coordinated to eight Fe's. These motifs pack in the face-sharing arrangement. This structure is the same as the $I4/mmm$ -type phases of Fe_2Mg [42] and Al_2S [43]. The calculated phonon spectrum confirms that this phase is dynamically stable at 1, 2, and 3 TPa with an electron temperature (T_{el}) of 8000 K as seen in Figs. 2(b)-2(d). Because the temperature at the core-mantle boundary of a super-Earth falls within the range from 4000 to 10 000 K [16], the choice of $T_{el} = 8000$ K is reasonable. Nevertheless, phonon dispersions with $T_{el} = 150$ K are also presented in Fig. S3 in the Supplemental Material [26], showing no imaginary frequencies in the entire Brillouin zone.

FeO . The phase with $Cmcm$ symmetry is the ground-state structure of FeO from 500 to 860 GPa (see Fig. S2(d) in the Supplemental Material [26]). From 860 GPa to 3 TPa, FeO stabilizes in the CsCl-type ($B2$) structure with $Pm\bar{3}m$ symmetry as shown in Fig. 3(a). Phonon calculations confirm its dynamic stability at 1, 2, and 3 TPa with $T_{el} = 8000$ K [Figs. 3(b)-3(d)]. At low electron temperature ($T_{el} = 150$ K), our calculated results show that it is also dynamically stable, as seen in Fig. S4 in the Supplemental Material [26].

Fe_3O_5 . From 575 to 1180 GPa, Fe_3O_5 adopts an orthorhombic phase with the $Pbam$ space group [see Fig. 1(b)]. In this structure, each Fe is eightfold coordinated by O's forming face-shared and edge/face diagonal-shared (an edge in one cube shares with a face diagonal of another cube)

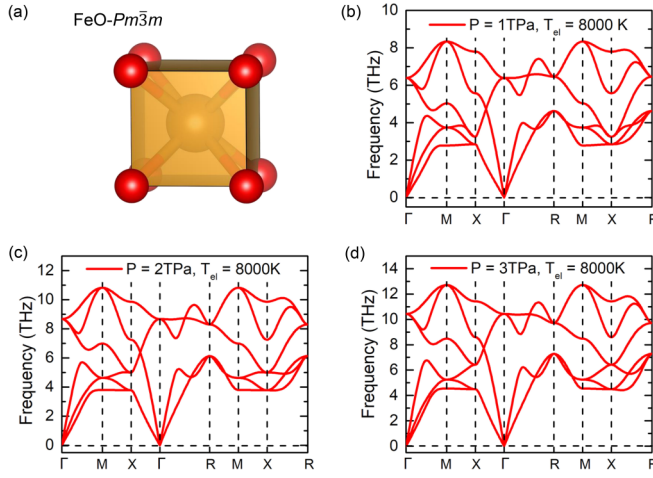


FIG. 3. (a) Crystal structure of $Pm\bar{3}m$ FeO. Fe and O atoms are denoted by light brown and red spheres, respectively. Phonon dispersions of $Pm\bar{3}m$ FeO with $T_{el} = 8000$ K at (b) 1 TPa, (c) 2 TPa, and (d) 3 TPa.

cubes, as seen in Fig. 4(a). The calculated phonon dispersion shows the $Pbam$ Fe_3O_5 is dynamically stable at 1 TPa with $T_{el} = 8000$ K [Fig. 4(b)] and $T_{el} = 150$ K (see Fig. S5 in the Supplemental Material [26]). At 1180 GPa, this structure decomposes into FeO and FeO_2 .

FeO_2 . The ground-state structure of FeO_2 is orthorhombic with $Pnma$ symmetry from 540 GPa to 3 TPa, as seen in Fig. 5(a). In this structure, each Fe is coordinated by eight O's forming distorted FeO_8 cubes. These cubes pack in a similar arrangement to that in $Pbam$ Fe_3O_5 . The dynamic stability of the $Pnma$ FeO_2 is verified by the absence of imaginary frequencies in the phonon dispersion at 1, 2, and 3 TPa with $T_{el} = 8000$ K as shown in Figs. 5(b)–5(d). Phonon dispersions with $T_{el} = 150$ K are shown in Fig. S6 in the Supplemental Material [26].

FeO_4 . Figure 6 plots the crystal structure and phonon dispersion for the FeO_4 with $P2_1/c$ symmetry. Each Fe is coordinated with eight O's to form edge-shared cubes. The calculated phonon dispersion shows this $P2_1/c$ FeO_4 phase is dynamically stable at 1 TPa with $T_{el} = 8000$ K [Fig. 6(b)] and $T_{el} = 150$ K (see Fig. S7 in the Supplemental Material [26]).

We performed the AIMD simulation to study the thermodynamical stability against melting for the five Fe-O ground

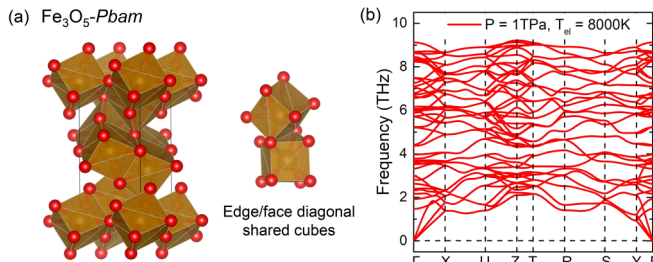


FIG. 4. (a) Crystal structure and edge/face diagonal-shared cubes of $Pbam$ Fe_3O_5 . Light brown and red spheres denote Fe and O, respectively. (b) Phonon dispersion of $Pbam$ Fe_3O_5 at 1 TPa with $T_{el} = 8000$ K.

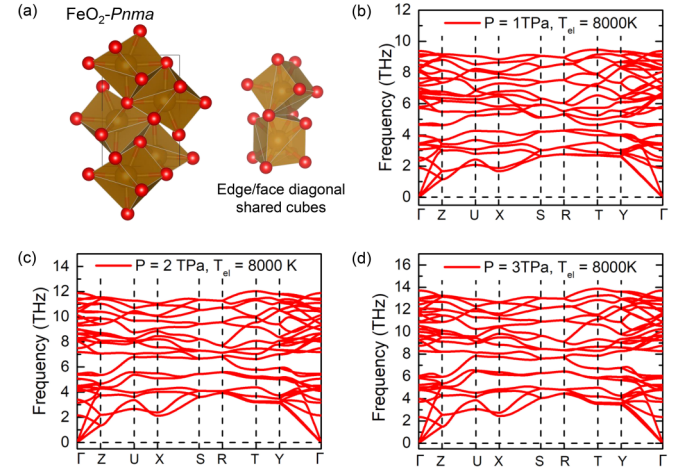


FIG. 5. (a) Crystal structure and edge/face diagonal-shared cubes of $Pnma$ FeO_2 . Light brown and red spheres denote Fe and O, respectively. Phonon dispersions of $Pnma$ FeO_2 at (b) 1 TPa, (c) 2 TPa, and (d) 3 TPa with $T_{el} = 8000$ K.

states. Both ion and electronic temperatures are 8000 K. This high temperature is close to the estimation of the super-Earth's interior [16]. The mean square displacement (MSD) and superposed atomic positions are shown in Fig. 7, which clearly describes the states in the simulation. During the AIMD, no melting was observed in Fe_2O and FeO from ~ 1 to 3 TPa. Therefore, the melting points of Fe_2O and FeO should be higher than 8000 K under these pressures. Fe_3O_5 does not show melting at ~ 1 TPa, either. When O content increases beyond Fe_3O_5 , the crystals start to melt. FeO_2 and FeO_4 both melt at 8000 K and ~ 1 TPa, but when pressure increased to 3 TPa, no melt was observed for FeO_2 . This is consistent with the general trend that the melting temperature increases with the increasing pressures, as shown in both Fe and FeO P - T diagram under low pressures [9,44]. At ~ 2 TPa, the FeO_2 does not melt in the simulation. However, its MSD shows a strong fluctuation. Therefore, the melting point of FeO_2 at ~ 2 TPa should be close to 8000 K. These AIMD simulations demonstrate the Fe-poor phases (i.e., FeO_2 and FeO_4) show lower melting points than the Fe-rich phases (Fe_2O and FeO). The Fe-rich phases can have very high melting points, larger than 8000 K at 1–3TPa. Therefore, these Fe-rich crystal phases can be stable under the conditions of the super-Earth's interiors.

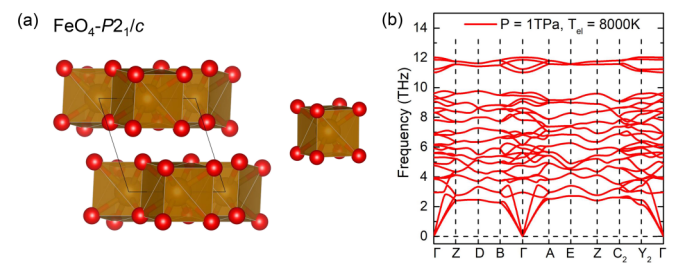


FIG. 6. (a) Crystal structure of $P2_1/c$ FeO_4 . Light brown and red spheres denote Fe and O, respectively. (b) Phonon dispersion of $P2_1/c$ FeO_4 at 1 TPa with $T_{el} = 8000$ K.

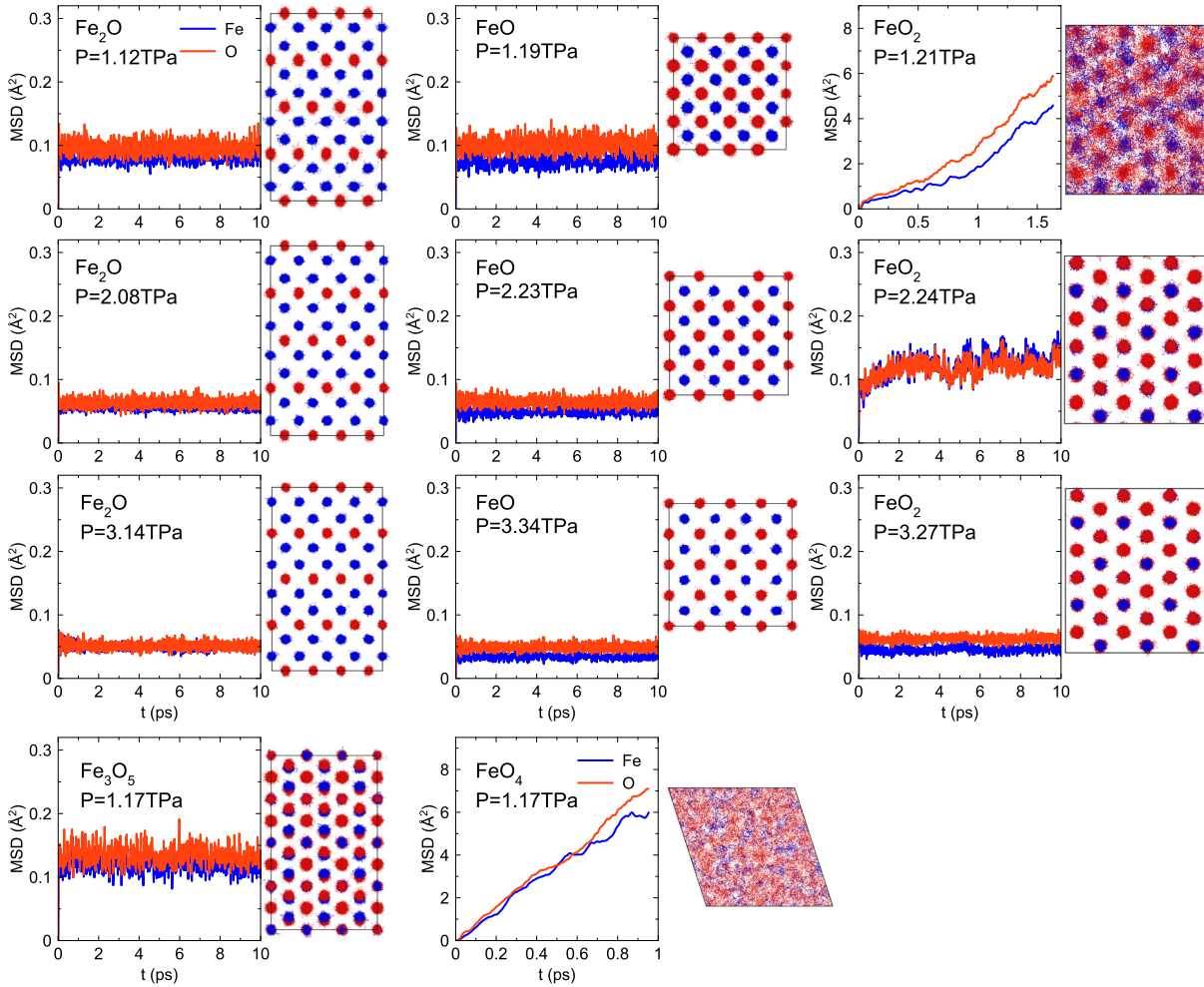


FIG. 7. Mean square displacement (MSD) of AIMD for ground states at $T = 8000$ K. The superposed atomic configurations shown along with the MSD are extracted from AIMD every five MD steps. Blue is Fe and red is O.

The electronic densities of states (DOS) at the Fermi level (E_F) of these five Fe-O compounds are investigated from 1 to 3 TPa. As shown in Fig. 8, our calculations indicate that, except for FeO_4 , all iron oxide phases identified are metallic. It has been reported that the FeO is a typical system that shows insulator to metal transition with increasing pressures. At ambient pressure, FeO shows an insulating $B1$ phase. When the pressure becomes larger than 120 GPa, the $B1$ phase transforms to the $B8$ phase, along with an insulator-metal transition and spin transition [45]. Then the FeO is always metallic at high pressure higher than 150 GPa [46]. Our current study is in the range of 1–3 TPa, and it is expected that most new FeO phases are metallic. For a given Fe_xO_y stoichiometry, results indicate that the carrier density decreases with increasing pressure. FeO_4 remains an insulating phase up to 3 TPa with band gap reduction, as seen in Fig. S12 in the Supplemental Material [26], despite the PBE/GGA gap underestimation. These results can be attributed to the enhancement of the overlap of the atomic wave functions as the pressure increases, which broadens the Fe d bands. As a result, the DOS spreads out in energies at higher pressures in all the crystal phases, as shown in Figs. S8–S12 in the Supplemental Material [26]. The d band broadening lowers the density of states at E_F , i.e.,

the carrier density. It also suppresses the net moment so that the system favors a nonmagnetic state as shown in Fig S1 in

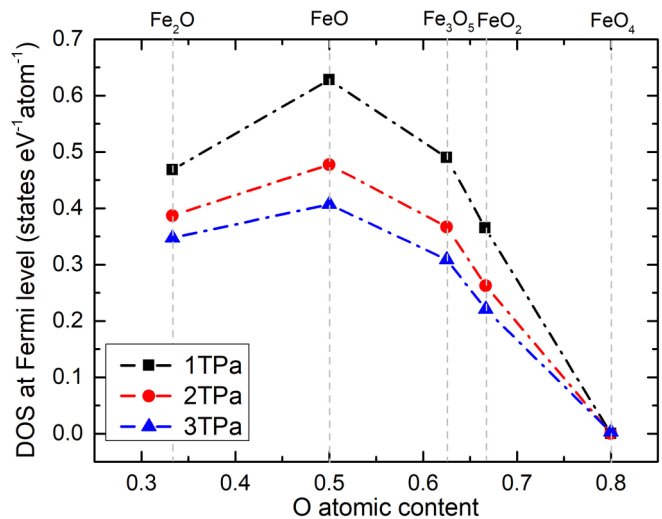


FIG. 8. Pressure variation of the carrier density in Fe-O compounds.

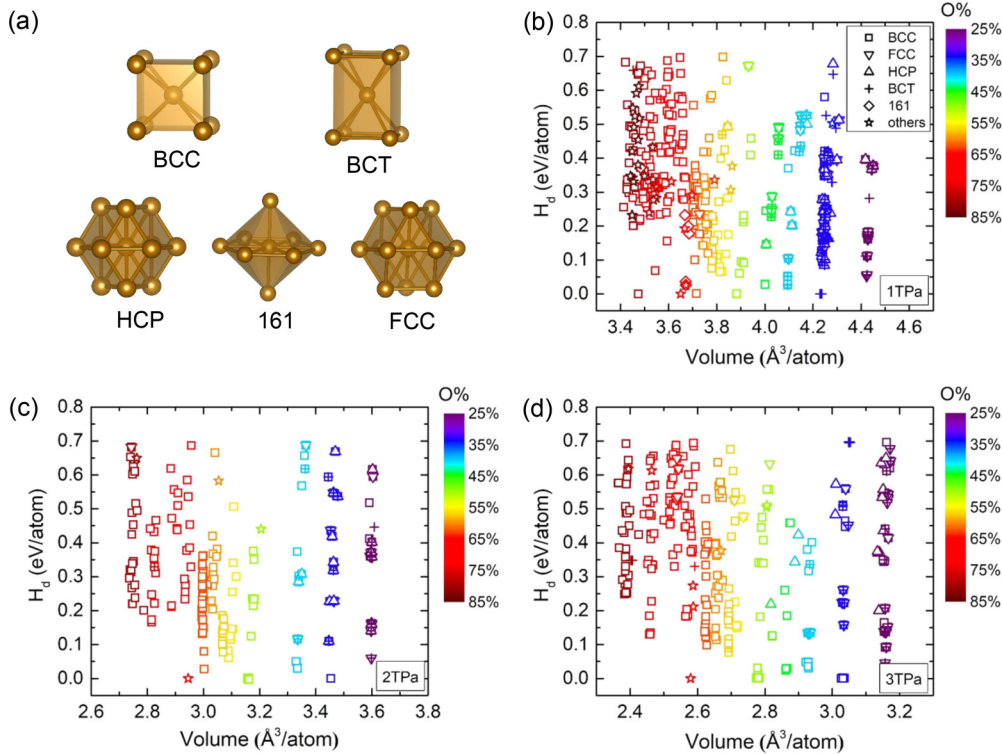


FIG. 9. (a) The template motifs considered here. (b)–(d) Enthalpies above the convex hull (H_d) of low-enthalpy Fe_xO_y structures vs their volumes at 1, 2, and 3 TPa. The symbols denote the local packing motifs, and colors represent oxygen concentration.

the Supplemental Material [26]. This mechanism is similar to the pressure effect on the magnet collapse of Fe [47]. For FeO_4 (shown in Fig. S12 in the Supplemental Material [26]), due to the increase in $3d$ bandwidth with pressure, the conduction band minimum moves closer to E_f and decreases the band gap. When the pressure is at 3 TPa, the band gap almost vanishes, indicating the FeO_4 almost becomes a metallic state. Overall, with the increase of pressure, the broadening of d bands promotes the transition from insulator to metal in FeO_4 and decreases carrier density for the metallic states with higher Fe contents.

C. Analysis of structure motifs of Fe-O system under pressure

Besides the stable Fe-O compounds, we also predicted several metastable structures in the Fe-O system from 1 to 3 TPa. Since the current calculation does not consider temperature effects on structural stability, these low-enthalpy metastable iron oxides may become stable at finite temperatures. Therefore, it is necessary to investigate structural motifs of these stable and metastable Fe_xO_y phases to reveal overall structural features in the Fe-O system at high pressures. Here, the threshold for metastability is set to their relative enthalpies (H_d) w.r.t. the convex hull by 0.7 eV/atom (~ 8000 K). The Fe-centered clusters in these iron oxides were defined by using the cluster alignment method [48]. Four typical motifs, including bcc, bct (body-centered tetragonal), fcc, and hcp are used as templates. We also include the “161” motif (two face-shared hexagonal caps), which is a common cluster in Fe-O binary compounds at high pressure [14]. Snapshots of these motifs are shown

in Fig. 9(a). We define an “alignment score” to quantify the similarity between aligned clusters and template motifs [37]. Here, the cutoff value of the alignment score is set to 0.125. If the alignment score is higher than 0.125, the cluster is marked as “others,” meaning the group of atoms cannot be classified into the current templates or is much more distorted than these perfect motifs.

Figures 9(b)–9(d) shows the relative enthalpies w.r.t. the convex hull of these stable and metastable iron oxides vs their volumes. The types of Fe-centered clusters and O concentrations are denoted with different symbols and colors, respectively. It can be found that, at 1, 2, and 3 TPa, several motifs may coexist in Fe-O compound structures with low O content, while, for iron oxides with higher O content, most of them adopt simple bcc motifs, as seen in Figs. 9(b)–9(d). Furthermore, we note that several motifs in iron oxides are determined as others at 1, 2, and 3 TPa. Some of them may form more complex clusters than the considered templates, some just highly distorted templatelike clusters, e.g., the ground-state $Pnma$ FeO_2 structure [Fig. 5(a)].

IV. CONCLUSIONS

In summary, we use the AGA method to study structure in the Fe-O system across a wide range of stoichiometries at 1, 2, and 3 TPa. Several stable phases with stoichiometries Fe_2O , FeO , Fe_3O_5 , FeO_2 , and FeO_4 are identified. The *ab initio* molecular dynamics simulations indicate that the Fe_2O and FeO phases have high melting points, larger than 8000 K at 1–3TPa. Therefore, these crystal phases can be stable under

the super-Earth's interior conditions. Fe_3O_5 is stable at 8000 K and 1 TPa. FeO_2 melts at 8000 K and 1 TPa while it remains stable at 8000 K and 3 TPa, indicating the melting point increases as a result of increasing pressure. Except for FeO_4 , the calculated electronic density of states shows these Fe-O compounds are metallic. As expected, the carrier density decreases with the increasing pressure. This is due to the enhancement of the overlap of the atomic wave functions at high pressure, which broadens the Fe d bands and lowers the density of states at E_f , i.e., the carrier density. The cluster alignment analysis reveals that most low-enthalpy phases prefer a bcc packing motif at high pressure, especially those with high O content. This study provides the structural database for the Fe-O system at ultrahigh pressure. To fully understand planetary interiors, the joint solubility of high-abundance elements such as Fe, Mg, O, and Si, etc., under high-pressure conditions must be addressed. For this purpose, the structural behavior of the binary, ternary, etc., systems need to be investigated first. Our study provides necessary information on Fe-O for developing the Fe-Mg-O phase diagram (also essential for the

quaternary phase diagram of Fe-Mg-Si-O). It is a preliminary step toward a better understanding of planetary interiors.

ACKNOWLEDGMENTS

Work at Xiamen University was supported by the National Natural Science Foundation of China (Grant No. 11874307). Work at Iowa State University and Columbia University was supported by the National Science Foundation Awards No. EAR-1918134 and No. EAR-1918126. We acknowledge the computer resources from the Extreme Science and Engineering Discovery Environment (XSEDE), which is supported by the National Science Foundation Grant No. ACI-1548562. B.D. is supported by JSPS KAKENHI Grant No. JP21K14656. R.W. was supported by the Guangdong Basic and Applied Basic Research Foundation (Grant No. 2021A1515110328). Molecular dynamics simulations were supported by the Numerical Materials Simulator supercomputer at the National Institute for Materials Science (NIMS).

-
- [1] A. E. Doyle, E. D. Young, B. Klein, B. Zuckerman, and H. E. Schlichting, *Science* **366**, 356 (2019).
 - [2] Y. W. Fei and H. K. Mao, *Science* **266**, 1678 (1994).
 - [3] M. P. Pasternak, S. Nasu, K. Wada, and S. Endo, *Phys. Rev. B* **50**, 6446 (1994).
 - [4] Y. W. Fei, D. J. Frost, H. K. Mao, C. T. Prewitt, and D. Hausermann, *Am. Mineral.* **84**, 203 (1999).
 - [5] G. K. Rozenberg, L. S. Dubrovinsky, M. P. Pasternak, O. Naaman, T. Le Bihan, and R. Ahuja, *Phys. Rev. B* **65**, 064112 (2002).
 - [6] J. Badro, G. Fiquet, V. V. Struzhkin, M. Somayazulu, H. K. Mao, G. Shen, and T. Le Bihan, *Phys. Rev. Lett.* **89**, 205504 (2002).
 - [7] S. H. Shim, A. Bengtson, D. Morgan, W. G. Sturhahn, K. Catai, J. Y. Zhao, M. Lerche, and V. Prakapenka, *Proc. Natl. Acad. Sci. USA* **106**, 5508 (2009).
 - [8] S. Ju, T. Y. Cai, H. S. Lu, and C. D. Gong, *J. Am. Chem. Soc.* **134**, 13780 (2012).
 - [9] H. Ozawa, F. Takahashi, K. Hirose, Y. Ohishi, and N. Hirao, *Science* **334**, 792 (2011).
 - [10] E. Bykova, L. Dubrovinsky, N. Dubrovinskaia, M. Bykov, C. McCammon, S. V. Ovsyannikov, H. P. Liermann, I. Kupenko, A. I. Chumakov, R. Ruffer *et al.*, *Nat. Commun.* **7**, 10661 (2016).
 - [11] B. Lavina, P. Dera, E. Kim, Y. Meng, R. T. Downs, P. F. Weck, S. R. Sutton, and Y. S. Zhao, *Proc. Natl. Acad. Sci. USA* **108**, 17281 (2011).
 - [12] B. Lavina and Y. Meng, *Sci. Adv.* **1**, e1400260 (2015).
 - [13] R. Sinmyo, E. Bykova, S. V. Ovsyannikov, C. McCammon, I. Kupenko, L. Ismailova, and L. Dubrovinsky, *Sci. Rep.* **6**, 32852 (2016).
 - [14] G. L. Weerasinghe, C. J. Pickard, and R. J. Needs, *J. Phys.: Condens. Matter* **27**, 455501 (2015).
 - [15] Q. Hu, D. Y. Kim, W. Yang, L. Yang, Y. Meng, L. Zhang, and H. K. Mao, *Nature (London)* **534**, 241 (2016).
 - [16] A. P. van den Berg, D. A. Yuen, K. Umemoto, M. H. G. Jacobs, and R. M. Wentzcovitch, *Icarus* **317**, 412 (2019).
 - [17] S. Seager, M. Kuchner, C. A. Hier-Majumder, and B. Militzer, *Astrophys. J.* **669**, 1279 (2007).
 - [18] S. Q. Wu, M. Ji, C. Z. Wang, M. C. Nguyen, X. Zhao, K. Umemoto, R. M. Wentzcovitch, and K. M. Ho, *J. Phys.: Condens. Matter* **26**, 035402 (2014).
 - [19] S. M. Foiles, M. I. Baskes, and M. S. Daw, *Phys. Rev. B* **33**, 7983 (1986).
 - [20] X. W. Zhou, R. A. Johnson, and H. N. G. Wadley, *Phys. Rev. B* **69**, 144113 (2004).
 - [21] A. Banerjea and J. R. Smith, *Phys. Rev. B* **37**, 6632 (1988).
 - [22] P. Brommer and F. Gahler, *Philos. Mag.* **86**, 753 (2006).
 - [23] P. Brommer and F. Gahler, *Modell. Simul. Mater. Sci. Eng.* **15**, 295 (2007).
 - [24] P. Giannozzi, S. Baroni, N. Bonini, M. Calandra, R. Car, C. Cavazzoni, D. Ceresoli, G. L. Chiarotti, M. Cococcioni, I. Dabo *et al.*, *J. Phys.: Condens. Matter* **21**, 395502 (2009).
 - [25] P. Giannozzi, O. Andreussi, T. Brumme, O. Bunau, M. Buongiorno Nardelli, M. Calandra, R. Car, C. Cavazzoni, D. Ceresoli, M. Cococcioni *et al.*, *J. Phys.: Condens. Matter* **29**, 465901 (2017).
 - [26] See Supplemental Material at <http://link.aps.org/supplemental/10.1103/PhysRevMaterials.6.043602> for crystallographic data of stable phases, enthalpies with the fixed magnetic moment, phonon spectra, the density of states, and comparison with all-electron calculations, which includes additional Ref. [27].
 - [27] The ELK code, <http://elk.sourceforge.net>.
 - [28] D. Vanderbilt, *Phys. Rev. B* **41**, 7892 (1990).
 - [29] K. Umemoto, R. M. Wentzcovitch, Y. G. Yu, and R. Requist, *Earth Planet. Sci. Lett.* **276**, 198 (2008).
 - [30] C. G. Broyden, *IMA J. Appl. Math.* **6**, 76 (1970).
 - [31] C. G. Broyden, *IMA J. Appl. Math.* **6**, 222 (1970).
 - [32] R. Fletcher, *Comput. J.* **13**, 317 (1970).
 - [33] D. Goldfarb, *Math. Comput.* **24**, 23 (1970).
 - [34] D. F. Shanno, *Math. Comput.* **24**, 647 (1970).
 - [35] A. Togo, F. Oba, and I. Tanaka, *Phys. Rev. B* **78**, 134106 (2008).
 - [36] A. Togo and I. Tanaka, *Scr. Mater.* **108**, 1 (2015).

- [37] S. Nosé, *J. Chem. Phys.* **81**, 511 (1984).
- [38] G. Kresse and D. Joubert, *Phys. Rev. B* **59**, 1758 (1999).
- [39] G. Kresse and J. Furthmüller, *Phys. Rev. B* **54**, 11169 (1996).
- [40] J. Sun, M. Martinez-Canales, D. D. Klug, C. J. Pickard, and R. J. Needs, *Phys. Rev. Lett.* **108**, 045503 (2012).
- [41] Y. Sun, M. Cococcioni, and R. M. Wentzcovitch, *Phys. Rev. Materials* **4**, 063605 (2020).
- [42] P. Gao, C. Su, S. Shao, S. Wang, P. Liu, S. Liu, and J. Lv, *New J. Chem.* **43**, 17403 (2019).
- [43] S. Shao, W. Zhu, J. Lv, Y. Wang, Y. Chen, and Y. Ma, *npj Comput. Mater.* **6**, 11 (2020).
- [44] S. Anzellini, A. Dewaele, M. Mezouar, P. Loubeyre, and G. Morard, *Science* **340**, 464 (2013).
- [45] H. Ozawa, K. Hirose, K. Ohta, H. Ishii, N. Hiraoka, Y. Ohishi, and Y. Seto, *Phys. Rev. B* **84**, 134417 (2011).
- [46] E. Greenberg, R. Nazarov, A. Landa, J. Ying, R. W. Hood, B. Hen, R. Jeanloz, V. B. Prakapenka, V. V. Struzhkin, G. Kh. Rozenberg *et al.*, *arXiv:2004.00652*.
- [47] V. Iota, J.-H. P. Klepeis, C.-S. Yoo, J. Lang, D. Haskel, and G. Srajer, *Appl. Phys. Lett.* **90**, 042505 (2007).
- [48] Y. Sun, F. Zhang, Z. Ye, Y. Zhang, X. Fang, Z. Ding, C. Z. Wang, M. I. Mendelev, R. T. Ott, M. J. Kramer *et al.*, *Sci. Rep.* **6**, 23734 (2016).